Evolution of Convective Energy and Inhibition before Instances of Large CAPE

PHILIP TUCKMAN,[a] VINCE AGARD,[a] AND KERRY EMANUEL[a]

[a] *Department of Earth, Atmospheric, and Planetary Sciences, Massachusetts Institute of Technology, Cambridge, Massachusetts*

(Manuscript received 21 November 2021, in final form 5 October 2022)

ABSTRACT: We analyze the evolution of convective available potential energy (CAPE) and convective inhibition (CIN) in the days leading up to episodes of high CAPE in North America. The widely accepted theory for CAPE buildup, known as the advection hypothesis, states that high moist static energy (MSE) parcels of air moving north from the Gulf of Mexico become trapped under warm but dry parcels moving east from over elevated dry terrain. If and when the resulting CIN erodes, severe convection can occur due to the large energy difference between the boundary layer parcels and cool air aloft. However, our results, obtained via backward Lagrangian tracking of parcels at locations of peak CAPE, show that large values of CAPE are generated mainly via boundary layer moistening in the days leading up to the time of peak CAPE, and that a large portion of this moisture buildup happens on the day of peak CAPE. On the other hand, the free-tropospheric temperature above these tracked parcels rarely changes significantly over the days leading up to such occurrences. In addition, the CIN that allows for this buildup of CAPE arises mostly from unusually strong boundary layer cooling the night before peak CAPE, and has a contribution from differential advection of unusually warm air above the boundary layer to form a capping inversion. These results have important implications for the climatology of severe convective events, as it emphasizes the role of surface properties and their gradients in the frequency and intensity of high CAPE occurrences.

SIGNIFICANCE STATEMENT: Severe convective events, such as thunderstorms, tornadoes, and hail storms, are among the most deadly and destructive weather systems. Although forecasters are quite good at predicting the probability of these events a few days in advance, there is currently no reliable seasonal prediction method of severe convection. We show that the buildup of energy for severe convection relies on both strong surface evaporation during the day of peak energy and anomalous cooling the night before. This progress represents a step toward understanding what controls the frequency of severe convective events on seasonal and longer time scales, including the effect of greenhouse gas–induced climate change.

KEYWORDS Atmosphere-land interaction; Deep convection; Storm environments; CAPE; Convective storms; Soil moisture

1. Introduction

Severe convective events, such as lightning strikes, strong straight-line winds, tornadoes, and hail are among the most deadly and destructive of weather phenomena. According to the International Disaster Database (emdat.be), convective storms caused a total of at least $314 billion (U.S. dollars; adjusted to 2021) of damage between 2001 and 2020 across more than 650 disasters worldwide.

It has been known for many years that these events usually occur when a column of air has abundant convective available potential energy (CAPE), sufficiently small convective inhibition (CIN), adequate wind shear, and a trigger to initiate convection (Bluestein 2007). The favorability of environments for severe convection (e.g., Grams et al. 2012), and the climatology of CAPE and CIN have also been studied (e.g., Riemann-Campe et al. 2009). Recently, this research has expanded to investigate the effect of climate change on severe convective events. Results suggest more convective events in North America during La Niña years (Allen et al. 2015; Cook et al. 2017), and several consequences of global warming, including more thunderstorms (e.g., Diffenbaugh et al. 2013; Romps et al. 2014; Seeley and Romps 2015; Allen 2018), more frequent or damaging hailstorms (e.g., Cao 2008; Changnon 2009; Botzen et al. 2010), an increase in tornado variability (e.g., Brooks et al. 2014), and an increase in the most severe events (e.g., Del Genio et al. 2007; Trapp and Hoogewind 2016; Hoogewind et al. 2017). Overall, models show that the frequency of environments favorable for convection (Trapp et al. 2007), the number of events (Gensini and Mote 2015), and crop damage (Rosenzweig et al. 2002) would increase with anthropogenic warming, but there are mixed views about whether these increases have occurred over the last few decades (Bouwer 2011; Kunkel et al. 2013). There are also studies that suggest there may be a decrease in the frequency of tornadoes with warming due to a decrease in wind shear (e.g., Brooks 2013). This body of work focuses on quantifying changing severe storm environments in global climate models and embedded regional models. Here, we focus on exploring the physical mechanisms that lead to high CAPE so as to better understand and predict how the frequency and severity of these events depend on climate, perhaps shedding light on how specific effects of climate change, such as nighttime warming,

Denotes content that is immediately available upon publication as open access.

Corresponding author: Philip Tuckman, ptuckman@mit.edu

DOI: 10.1175/MWR-D-21-0302.1

affect convective events (e.g., Dessens 1995), or how other environmental features, such as soil moisture, affect the climatology of these events (e.g., Schär et al. 1999).

While severe convection usually requires both high CAPE and sufficiently strong wind shear, there are cases of severe convection and even tornadoes in low CAPE environments (e.g., Sherburn and Parker 2014). The most severe convective storms, however, occur in high CAPE environments, and it is worth understanding how this high CAPE comes about.

Currently, the main theory of how CAPE develops in midlatitudes is the advection hypothesis, which states that differential advection of warm, moist air under warm, dry air leads to the buildup of CAPE (Carlson and Ludlam 1968; Carlson et al. 1983; Yang and Shu 1985; Emanuel 1994). For example, in North America, warm, moist air moving north from the Gulf of Mexico can move and be trapped underneath warm, dry air moving east from elevated dry regions, causing an abundance of both CAPE and CIN. Then, when the CIN becomes small enough, the CAPE is released in convective events. In this framework, the relevant potential energy comes from the difference between warm, moist air moving north from the Gulf and the colder air aloft.

Here, we show that extreme CAPE values over North America are due to increases of moist static energy (MSE) of boundary layer parcels in the days leading up to the time of peak CAPE, with a large portion of this increase happening on the day of peak CAPE. In addition, we show that the buildup of CIN required for MSE to build up is due mostly to unusually strong boundary layer cooling the night before the CAPE peak, while the decrease in CIN just before a high CAPE occurrence is usually due to boundary layer sensible heating. The abundance of CIN before the day of a high CAPE occurrence allows for the buildup of boundary layer energy without the energy being released immediately through shallow convection.

The rest of the paper is organized as follows. In section 2, we discuss the methods used to analyze the relevant quantities before the time of peak CAPE. Next, in section 3, we present five case studies meant to represent different patterns of CAPE development, then show the statistical distributions of relevant quantities for many more occurrences to reach conclusions about the usual patterns of CAPE buildup and CIN behavior. This section includes comparing high and low CAPE cases to understand what differentiates occurrences of very large CAPE. Last, in section 4, we discuss the implications of these findings and directions of possible future research. The appendices address methodological issues, specifically the choice of the dataset used (appendix A) and what constitutes a high CAPE occurrence (appendix B).

2. Methods

We use North Atlantic Regional Reanalysis (NARR) data from Mesinger et al. (2006) to study the proximate cause of anomalously high CAPE occurrences. This dataset has a time resolution of 3 h, a horizontal resolution of about 32 km, and 29 pressure levels. The capability of this resolution to capture the relevant phenomena is discussed in appendix A. The procedure used to analyze the data consists of five main steps. First, we identify regions and times with anomalously high CAPE. Second, the boundary layer (25 hPa above the surface) parcels at the regions and times of maximum CAPE are subjected to a back-trajectory analysis to determine their paths and thermodynamic properties before the identified occurrence. Third, we perform back-trajectory analyses on parcels in the capping inversion at the time of maximum convective inhibition, as described in detail later in this section. Fourth, the properties of "seen" air parcels, i.e., parcels at the same horizontal location as the boundary layer parcels at an intermediate altitude (that of the most negative buoyancy) and at 500 hPa, are calculated. Finally, the evolutions of properties leading to "high CAPE cases" (final CAPE > 1.75 kJ kg^{-1}) and "low CAPE cases" (final CAPE < 1 kJ kg^{-1} and >0.75 kJ kg^{-1}) are compared to understand what leads to anomalously high CAPE. The methods used in each of these steps are now described in detail.

The first step in identifying high CAPE occurrences is to calculate CAPE with respect to parcels lifted from 25 hPa above the surface everywhere in the region of interest (latitude greater than 36°, longitude between −120° and −74°) at each time step. The altitude from which to lift parcels is chosen so as to be representative of the boundary layer without being so close to the surface that the parcels' properties, including wind, would be unrepresentative of the whole boundary layer. The time period studied is from 1 March to 31 August, in 2012 and 2013. The CAPE values are smoothed with respect to the two spatial dimensions with a Gaussian filter. All points that have a smoothed CAPE larger than any other point within a 640 km × 640 km × 36 h region and have a peak (non-smoothed) CAPE larger than 1.75 kJ kg^{-1} (discussed in appendix B) are identified as high CAPE cases. Occurrences with peak CAPE between 0.75 and 1 kJ kg^{-1} are identified as low CAPE cases and serve as a basis for comparison. It is important to note that this process does not identify severe convective events, just occurrences of large CAPE, usually a necessary but insufficient condition for severe convection.

Once CAPE peaks are identified, a back-trajectory analysis is executed. To ensure stable statistics, we track not just one air parcel but the 18 parcels with the highest CAPE in the region of the CAPE peak. We use a time step of $\Delta t = -15$ min (briefly discussed in appendix A), and during the period of tracking we assume that the position of the air parcel is given by

$$\mathbf{x}(t + \Delta t) = \mathbf{x}(t) + \Delta t \mathbf{u}(t), \tag{1}$$

where $\mathbf{x}$ is the three-dimensional position and the velocity ($\mathbf{u}$) consists of zonal, meridional, and pressure components. The velocity is interpolated in space and time from NARR data via a multilinear polynomial interpolator. This formula is applied to the 18 identified boundary layer parcels until we reach approximately noon local time more than 6 days before the time of peak CAPE (which almost always occurs between noon and midnight inclusive).

Since we wish to understand the buildup of CIN as well as the buildup of CAPE, we also track intermediate altitude parcels that were above the boundary layer parcels at the time of maximum virtual potential temperature difference between

the lifted parcel and its environment (a proxy for CIN—discussed later in this section) for the 6 days before the high CAPE occurrence (using the same method as above). This allows us to understand whether the virtual potential temperature difference (and therefore the CIN) grows due to differential advection (in which case the tracked parcels would have relatively constant virtual potential temperature over time), boundary layer cooling, or heating of midlevel parcels (in which case the virtual potential temperature of the tracked parcels would increase as CIN builds up).

Once parcels have been tracked, we calculate their properties as a function of time. We linearly interpolate (with a multilinear polynomial) data fields from the NARR to calculate the temperature, geopotential height, and specific humidity of all tracked parcels. In addition, we identify properties of "seen parcels," i.e., parcels at pressure levels of interest and the same horizontal position as the tracked boundary layer parcels. These parcels are important as they help define the buoyancy of lifted parcels. Specifically, the boundary layer parcels need to be positively buoyant (or nearly so) with respect to the seen column for there to be convection, and the maximum updraft velocity is controlled by how positively buoyant the boundary layer parcels are. All quantities shown are averages across the 18 identified parcels, with the most extreme value on each side being excluded.

We use these properties to calculate several composite quantities, including the moist static energy (MSE) of the boundary layer parcels, the saturation MSE (with saturation denoted by *; i.e., MSE*) of the seen 500-hPa parcels, the virtual potential temperature of the boundary layer parcels lifted to an intermediate altitude (discussed below), and the virtual potential temperature of the seen intermediate altitude parcels.

The MSE and MSE* are given by

$$\mathrm{MSE} = C_p T + gz + Lq, \tag{2}$$

$$\mathrm{MSE}^* = C_p T + gz + Lq^*, \tag{3}$$

where $C_p \equiv 1005$ J kg^{-1} K^{-1} is the specific heat of air at constant pressure, T is the temperature (K), $g \equiv 9.8$ m s^{-2} is the gravitational acceleration, z is the geopotential height, $L \equiv 2\,500\,000$ J kg^{-1} is the latent heat of vaporization of liquid water, q is the specific humidity, and q^* is the saturation specific humidity. This allows us to define a latent heat (Lq) and a dry static energy (DSE $\equiv C_p T + gz$, also referred to as sensible heat). We also define a proxy for CAPE:

$$\mathrm{PCAPE} \equiv \mathrm{MSE}_{\mathrm{B.L.}} - \mathrm{MSE}^*_{500\mathrm{hPa}}, \tag{4}$$

as the difference between the boundary layer MSE and the seen MSE* at 500 hPa.

The virtual potential temperature (θ_V) of parcels is calculated as the virtual temperature of a parcel displaced dry adiabatically to a reference pressure (1000 hPa), and the lifted θ_V is the θ_V that a boundary layer parcel would have if it were lifted to the level in question along a dry adiabat until saturation, then along a reversible moist adiabat. At each time step, the lifted θ_V and θ_V above the boundary layer parcel are calculated at each pressure level. The level chosen as the "intermediate" altitude is the level (between 600 and 900 hPa) at which the environmental θ_V minus the lifted θ_V is largest, i.e., the level at which the boundary layer parcel would be the most negatively buoyant. We define a proxy for CIN:

$$\mathrm{PCIN} \equiv \max(\theta_V - \theta_{V,\mathrm{lifted}}), \tag{5}$$

as the difference between the lifted θ_V and seen θ_V where the maximum is taken between 600 and 900 hPa.

For both the CAPE and CIN, it is useful to use proxies (PCAPE and PCIN) rather than the CAPE and CIN themselves, as they allow us to use back trajectories of the respective parcels to understand how the CAPE and CIN evolves.

Next, the time before each high CAPE occurrence is divided into periods to better understand the lead-up to anomalously high CAPE. The MSE time series are divided into "early" and "late" periods, with the time of minimum PCAPE within 18 h before peak CAPE chosen as the dividing time. This time is chosen as the onset of final CAPE build up. The θ_V time series are divided into "early," "middle," and "late" periods, where the middle period corresponds to the buildup of CIN and the late period corresponds to its disappearance. The dividing line between middle and late is chosen as the time of maximum PCIN within 18 h before peak CAPE. The beginning of the middle period is defined as the most recent time before the end of the middle period that PCIN is less than 1.5 K and is at a local minimum. If such a time does not exist between the beginning of the late period and noon between 6 and 7 days before the time of high CAPE, then the time of minimum PCIN is chosen. The beginning of the early period is 24 h before this.

Finally, high and low CAPE cases are compared. The averages of all relevant quantities as a function of time before peak CAPE are calculated for high and low CAPE cases separately, and the difference between these averages are taken as the differentiating factors of anomalously large CAPE cases.

3. Results

In this section, we first present five examples, then discuss the statistics of relevant quantities across the 221 high (CAPE $>$ 1.75 kJ kg^{-1}) and 188 low (CAPE $<$ 1 kJ kg^{-1} and CAPE $>$ 0.75 kJ kg^{-1}) CAPE cases studied.

The first example corresponds to typical high CAPE occurrence and the second to a typical low CAPE occurrence. The third example is a high CAPE case with particularly strong boundary layer heating and the fourth is a case that fits the advection hypothesis. Finally, the fifth case is one in which the boundary layer air starts out cold, well to the north of the location of peak CAPE. The choices of these cases are justified in section 3b. For each example, we present boundary layer and "seen" properties—the properties of the parcels above and at the same horizontal position as the boundary layer parcels. After each example is presented and discussed, the quantities that differentiate high and low CAPE cases are discussed, and the distributions of relevant quantities are shown. These

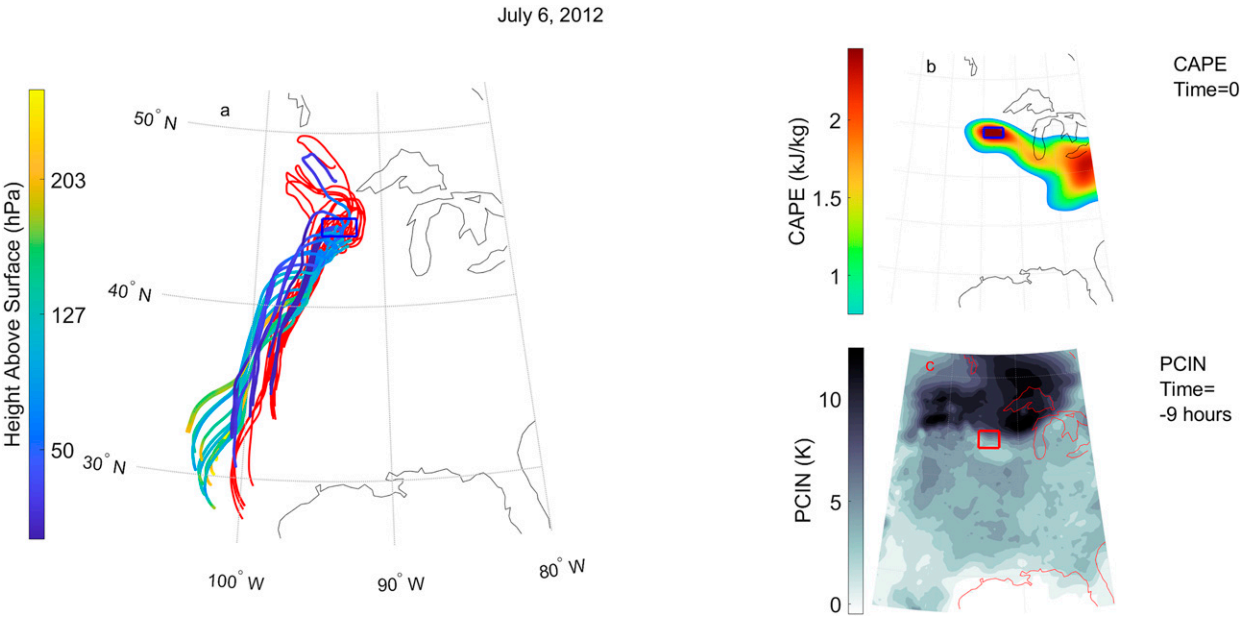

FIG. 1. Trajectories of relevant air parcels for the first example and maps of CAPE and PCIN at relevant times. The blue rectangles in (a) and (b) show the location of the boundary layer parcels when CAPE peaks. (a) Trajectories of the parcels that arrive in the boundary layer (25 hPa above the surface) at the position and time of maximum CAPE (red) and trajectories of the parcels that are at the position, time, and altitude of maximum PCIN (blue–green–yellow). These trajectories change color corresponding to the altitude of these tracked parcels, according to the scale on the left. The trajectories go from the beginning of the early period (defined in section 2) until the time of high CAPE, which in this case is about 65 h. (b) Smoothed CAPE at the time of maximum CAPE, with the same blue rectangle as in (a). (c) PCIN at the time of maximum PCIN, with a red rectangle around the positions of the boundary layer parcels at that time.

distributions show what usually causes abnormally high CAPE, and the buildup and disappearance of the CIN that is necessary for this CAPE build up.

a. Examples

We first present an example whose CAPE behavior is typical of those in the dataset (see discussion in section 3b). The air movement leading to this high CAPE occurrence is shown in Fig. 1, and the time evolution of relevant properties is shown in Fig. 2.

This high CAPE example occurs just west of the Great Lakes. The various parcels in the boundary layer at the time of maximum CAPE do not all follow the same path in the 65 h before the occurrence; some of the parcels come from the north and some from the south (red lines in Fig. 1a). These parcels were nearly all within 25 hPa of the surface for 60 h before the high CAPE occurrence (not shown). The mid-level parcels that arrive at the capping inversion at the time of maximum PCIN similarly arrive from different locations (blue–green–yellow lines in Fig. 1a). The spatial pattern of CAPE at the time of the high CAPE occurrence is shown in Fig. 1b. There is a clear maximum of smoothed CAPE (~2.5 kJ kg^{-1}) in the region studied (by design), and the blue rectangle (in Figs. 1a,b) shows the final positions of the boundary layer parcels studied. The pattern of PCIN at the time of maximum PCIN (in this case 12 h before the time of maximum CAPE) is shown in Fig. 1c. There is some PCIN (~8 K) in the region of the boundary layer parcels at this time, shown with a red rectangle. There is much more PCIN elsewhere, to the north, but these regions of high CIN do not lead to a buildup of as much CAPE as the region in question (Fig. 1b). The similarity in location of the rectangles in Figs. 1b and 1c show that there is little movement of the boundary layer parcels in the 12 h before the high CAPE occurrence.

Figure 2 shows the evolution of relevant quantities in the days before peak CAPE. Figure 2b shows the quantities relevant to the buildup of CAPE. The boundary layer MSE (red line), has a diurnal cycle that slowly increases from 3 days to 9 h before peak CAPE. The diurnal cycle on the days before peak CAPE have an average amplitude of about 5 kJ kg^{-1}. Then, in the 9 h before peak CAPE, the MSE increases by about 15 kJ kg^{-1}. The sensible heat component of the boundary layer MSE has a diurnal cycle that does not change significantly, while the latent energy increases in the days leading up to the time of peak CAPE, driving the overall behavior of the boundary layer MSE. In contrast, the seen MSE* at 500 hPa (blue line) does not have large systematic changes in the days before peak CAPE. This indicates that boundary layer heating (specifically via an increase in latent energy) is the most significant factor in the increase in PCAPE for this high CAPE case. The relationship between PCAPE, our proxy for CAPE, and CAPE itself, is shown in Fig. 2a (dashed red line and solid red line). While the two quantities are not exactly proportional, the change in the quantities almost always have the same sign and have the same pattern, following a diurnal cycle on the day before the CAPE peak and increasing dramatically on the day of the peak.

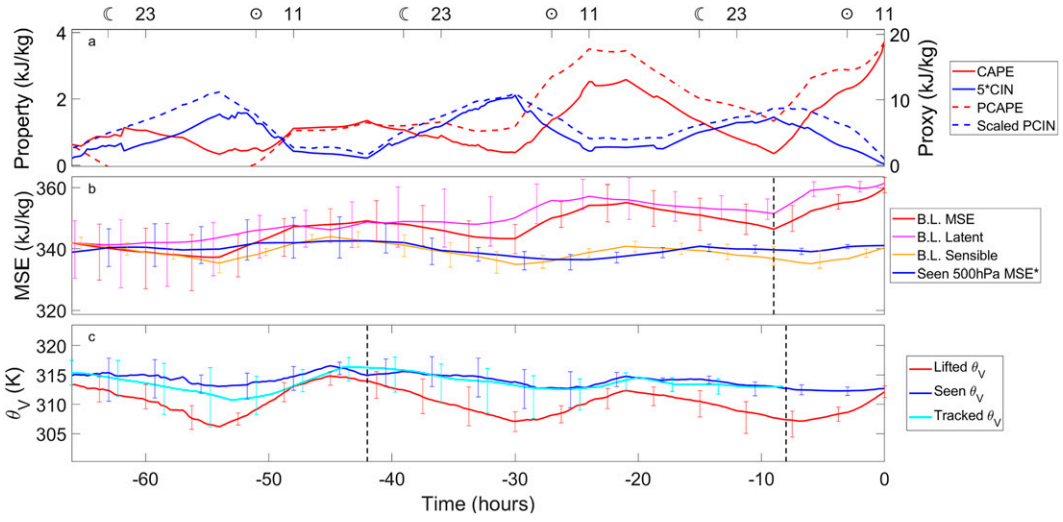

FIG. 2. Time evolution of relevant properties over the 65 h before the time of maximum CAPE, chosen as 24 h before the beginning of CIN buildup. (a) Convective properties, CAPE (red) and CIN (blue), as well as their proxies, PCAPE (dotted red) and PCIN (dotted blue), for the boundary layer parcels. The CIN is multiplied by 5 for ease of viewing. The PCIN time series is scaled by $50gH/300$ K, where g is the acceleration of gravity, H is the approximate height of the capping inversion (1 km), and 300 K is a typical value of θ_V. (b) Boundary layer MSE (red), MSE* at 500 hPa at the horizontal location of the boundary layer parcel (blue), and the sensible (orange) and latent (pink) components of boundary layer MSE. Each component of the MSE is shifted so that its starting value is the same as that of the total boundary layer MSE, making the quantities easier to compare. (c) Lifted boundary layer θ_V (red), θ_V at the level of maximum virtual potential temperature difference at the horizontal location of the boundary layer parcel (blue), and tracked θ_V (cyan). All error bars correspond to the 10th and 90th percentiles of the 18 parcels. The vertical dashed line in (b) represents the division between the "early" and "late" periods—chosen as the time of minimum PCAPE. The first vertical dashed line in (c) represents the division between the "early" and "middle" periods—chosen as the beginning of PCIN buildup, and the second vertical dashed line represents the division between the "middle" and "late" periods—chosen as the time of maximum PCIN. The symbols at the top of the plot represent approximate local sunset (☾) and sunrise (⊙) while the numbers are approximate local times.

Figure 2c shows the quantities relevant to the buildup and decrease of CIN. The seen θ_V at the level for which *P*CIN is largest is shown in blue, while the θ_V of the boundary layer parcels lifted to that level is shown in red. In addition, the θ_V of the parcels that form the capping inversion, i.e., the parcels above the boundary layer parcels at the time of maximum CIN, is shown in cyan. Overall, the lifted and seen θ_V both have a diurnal cycle, with the changes in lifted θ_V having a much larger amplitude. In this example, CIN builds up over the 2 days before the CAPE peak—i.e., CIN was very small about 42 h before the CAPE peak, and small but nonzero 22 h before. During the two nights before the CAPE peak, the boundary layer parcels cool significantly more than the seen parcels, leading to a large PCIN. The tracked θ_V follows the seen θ_V, but neither change is particularly important to the buildup of CIN, as changes in lifted θ_V dominate. In the final 6 h before the high CAPE occurrence, the boundary layer parcels heat much more than the seen parcels, causing PCIN to decrease to zero. This means that the decay of the capping inversion is due to boundary layer heating, matching the increase in boundary layer sensible heat (Fig. 2b). These trends in PCIN (dashed blue line in Fig. 2a) are reflected in the measured CIN (solid blue line in Fig. 2a), indicating that it is a good proxy.

Figures 3 and 4 show the second example, a typical low CAPE case. This example occurred at high latitudes, well north of the Great Lakes, and has a relatively small amount of peak (smoothed) CAPE, only about 0.5 kJ kg^{-1} (Fig. 3b). The parcels that were in the boundary layer at this point came immediately from the northwest, and before that from the southwest. The boundary layer parcels were within 60 hPa of the surface for 50 h before the time of maximum CAPE (not shown). The parcels that formed the capping inversion follow a similar trajectory, but started farther north than the boundary layer parcels. At the time of maximum PCIN (−15 h), there is some but not a huge amount of inhibition nearly everywhere (Fig. 3c).

The evolutions of relevant quantities for this case are shown in Fig. 4. Over the 48 h before the CAPE peak, the boundary layer MSE increases slightly, by about 5 kJ kg^{-1} (Fig. 4b). The seen parcels cool by about the same amount. The final PCAPE of less than 6 kJ kg^{-1} is much smaller than the equivalent 20 kJ kg^{-1} from the first example. The small increase in boundary layer MSE is mostly controlled by the latent energy, while the sensible heat follows a relatively weak diurnal cycle, changing by only a few kilojoules per kilogram. Figure 4a shows the measured CAPE, and aside from when it is zero due to the boundary layer parcels being negatively buoyant with respect to the whole column (between −4 and −5 and between −25 and −20 h), the MSE difference is a reasonably good proxy for it.

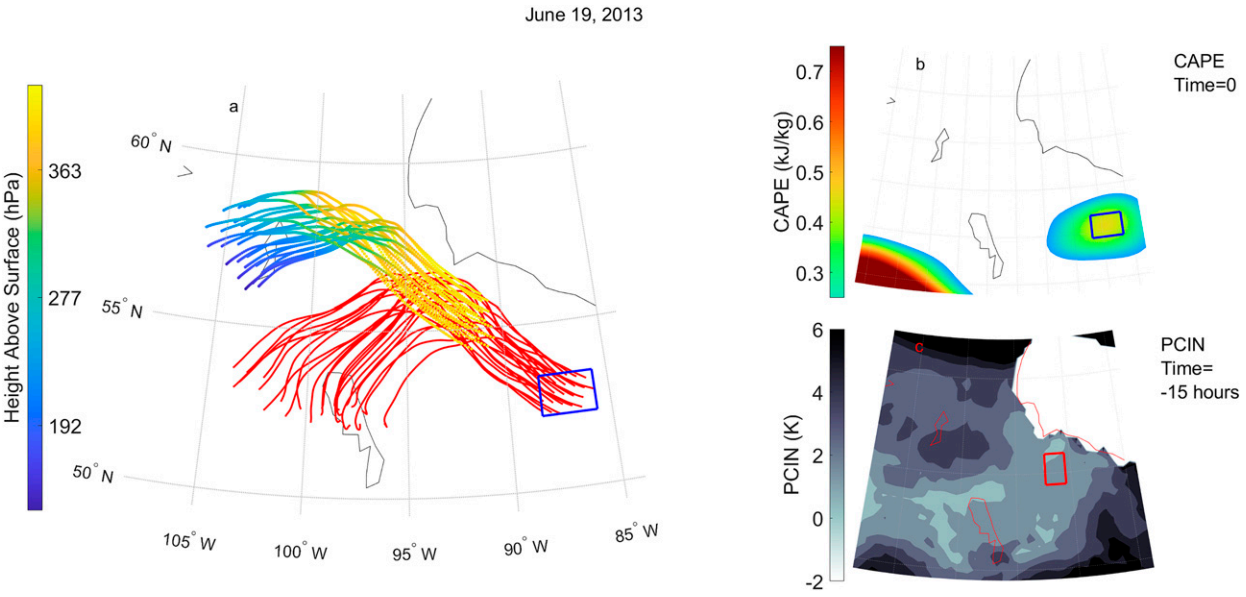

FIG. 3. As in Fig. 1, but for the second case studied. The trajectories extend back in time 48 h.

Figure 4c shows the quantities relevant for CIN behavior for this case. The most striking feature of these time series is that there is rarely any significant *P*CIN, and therefore almost never a significant amount of CIN. Although the lifted and seen θ_V seem to be rising and falling, this is due to the capping inversion changing altitude, not the energetics of the relevant parcels. Because the magnitude of PCIN is small, its exact altitude is not particularly meaningful and is more variable than usual. This can be seen by comparing the movement of those two quantities, defined at a variable altitude, to the more directly tracked quantities, the tracked θ_V and boundary layer θ_V. We regard this case as typical of most summertime continental convection. The absence of any significant CIN makes such cases more similar to quasi-equilibrium convection, but with lags owing to the diurnal cycle.

The third case is shown in Figs. 5 and 6. This example is a case with particularly strong boundary layer heating during the day of peak CAPE and has the largest CAPE of any of the cases analyzed (see CAPE distributions in appendix B). It is also a case for which CIN exists over a long period before the time of peak CAPE (almost 100 h) due to both boundary layer cooling and advection under warm air. The paths of the boundary layer parcels (Fig. 5a) are more similar to each other than those of the first example. The parcels, which end

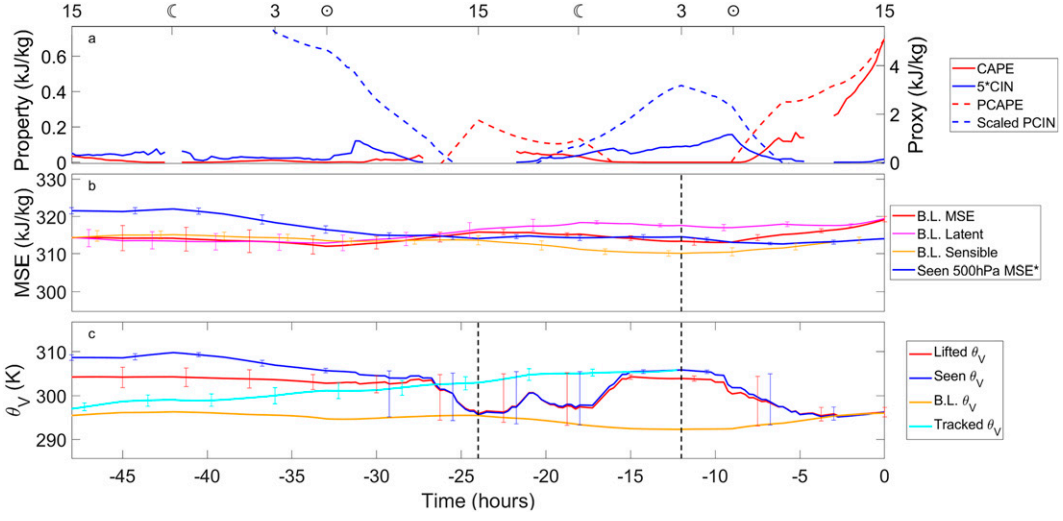

FIG. 4. (a)–(c) As in Fig. 2, but for the second case. If the lifted parcel is negatively buoyant everywhere in the column, CAPE is zero, CIN is undefined, and both are, therefore, not shown. In addition, the boundary layer θ_V [orange line in (c)] is shown to demonstrate that the altitude of the capping inversion is changing.

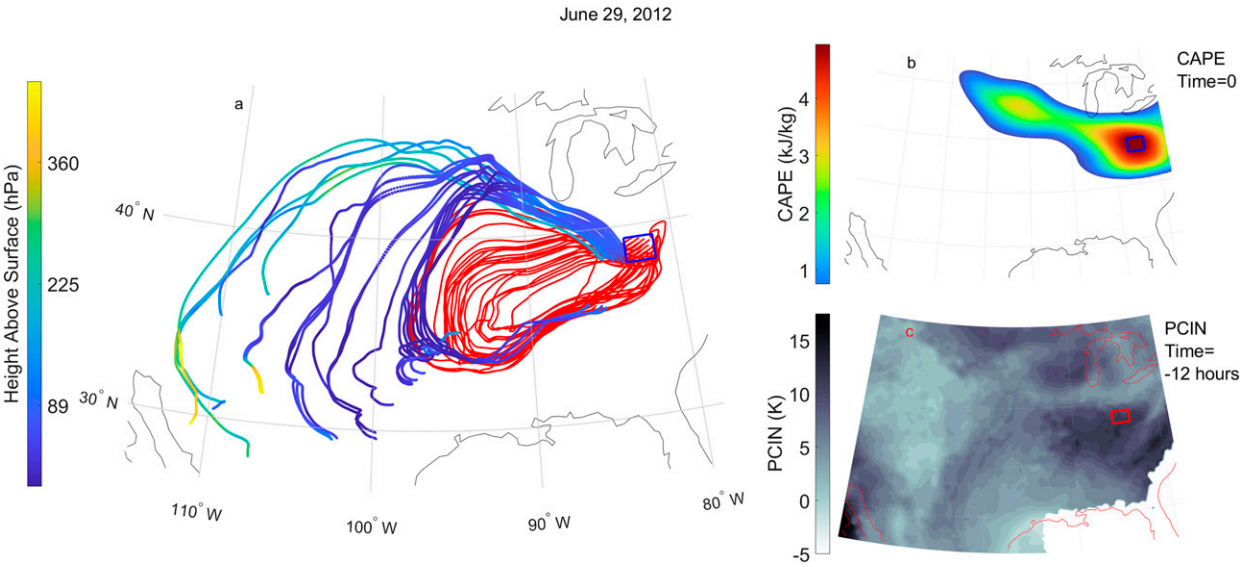

FIG. 5. As in Fig. 1, but for the third high CAPE example. The time series extend back about 120 h, since CIN buildup begins almost 100 h before the time of high CAPE.

up just south of the Great Lakes, had traveled in a large loop over the days before peak CAPE, moving first southwest, then north, then east. These parcels were between 950 and 970 hPa at the time of high CAPE, and the vast majority of them were within 50 hPa of the surface for 80 h prior to this (not shown). The midlevel parcels (blue–green–yellow lines in Fig. 5a) had traveled together from the northwest, and, before that, from the southwest. The high CAPE area, shown in Fig. 5b, is unusually large, both in spatial extent and amount of CAPE. The smoothed CAPE is around 5 kJ kg^{-1} in the area of interest, and there is a significant amount of CAPE for a few degrees longitude and latitude around the peak. During the night before peak CAPE (at −12 h), there was well over 10 K of PCIN at the location of the parcels in question, shown in Fig. 5c.

The evolution of relevant quantities for the third case is shown in Fig. 6. The most striking of these is the boundary layer MSE, shown in red in Fig. 6b. For the 4 days before the peak, the MSE follows a diurnal cycle, with an amplitude of roughly 10 kJ kg^{-1} and an overall increasing trend. Then, on the day of the high CAPE occurrence, the boundary layer MSE increases by almost 30 kJ kg^{-1} in about 8 h, double the 15 kJ kg^{-1} from the first case. The diurnal cycle of boundary layer MSE is mostly owing to variations in sensible heat content (orange line), but it is the latent energy (pink) that increases dramatically on the day of peak CAPE. Both quantities increase over the 4 days before peak CAPE. Meanwhile, the range of the seen 500-hPa MSE* is about 5 kJ kg^{-1} over the 120 h before the time of maximum CAPE. This means that the changes in PCAPE, shown in Fig. 6a as a red dashed line,

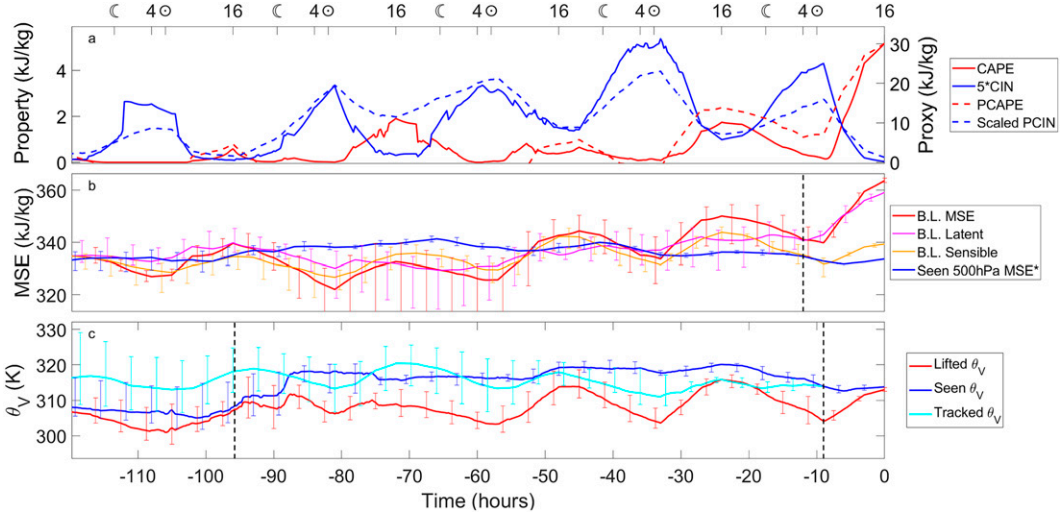

FIG. 6. As in Fig. 2, but for the third example high CAPE occurrence.

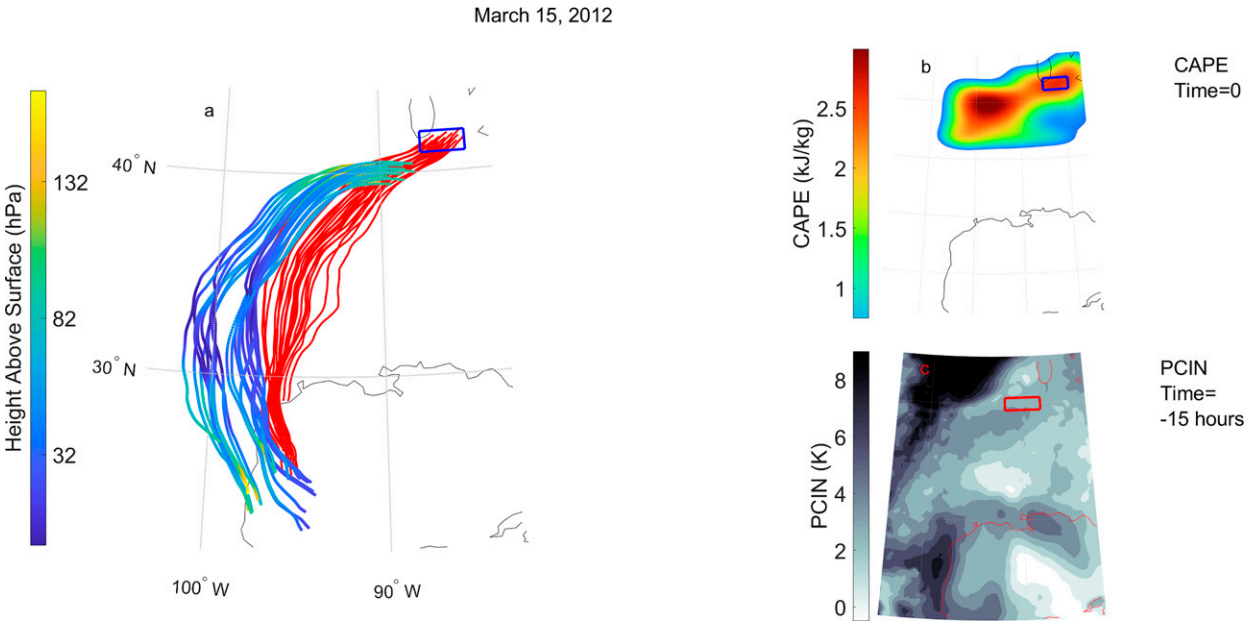

FIG. 7. As in Fig. 1, but for the fourth high CAPE example. The trajectories extend back about 72 h.

are controlled mostly by the changes in boundary layer MSE. In this example, as in the first one, the CAPE (red solid line in Fig. 6b) is not proportional to PCAPE, but follows the same general pattern. Specifically, the CAPE and the PCAPE both exhibit a very large and very fast increase on the day of peak CAPE. Both quantities also exhibit a significant bump on the day before the high CAPE occurrence.

The quantities relevant for the evolution of CIN in the second example occurrence are shown in Fig. 6c. To find a time where the boundary layer parcels were not trapped underneath warmer air, i.e., PCIN was small, we have to go all the way back to 96 h before the time of peak CAPE. Between that time (−96 h) and the next day (−65 h), the seen PCIN increases significantly, indicating that the boundary layer parcels are advected underneath warmer air. The capping inversion also becomes drier and its altitude increases (from 825 to 650 hPa, not shown) at around −89 h. After that, the lifted θ_V follows a diurnal cycle, while the seen θ_V is relatively constant up until the night before peak CAPE (−22 to −10 h). During that time, the seen θ_V and the lifted θ_V decrease dramatically. Then, on the day of peak CAPE, the lifted θ_V increases, corresponding to the increase in boundary layer MSE. The tracked θ_V does not change similarly to the seen θ_V in the middle period, indicating that relative advection, not heating/cooling of midlevel parcels, controls the seen θ_V. Overall, the CIN in this example seems to be caused by differential advection underneath warm air or subsidence into the capping inversion many days before the CAPE peak. Figure 6a shows that PCIN is a decent proxy for CIN in this example, as they both undergo a diurnal cycle with a maximum at −36 h and decrease to zero on the day of peak CAPE.

Figures 7 and 8 show the fourth high CAPE example, chosen as a case that partially fits the advection hypothesis in that the cooling of the seen 500-hPa parcels is comparable to the warming of the boundary layer parcels. The trajectories of the boundary layer parcels are shown in red in Fig. 7a. As the advection hypothesis would predict, the parcels are moving north from the Gulf of Mexico. These parcels were at about 960 hPa at the time of peak CAPE, and were within 25 hPa of the surface for 50 h prior to that (not shown). The midlevel parcels (blue–green–yellow lines in Fig. 7a) are also moving north from the same region. The spatial extent of nonzero CAPE, shown in Fig. 7b, is much larger than usual, but the peak is not unusually large; the maximum CAPE values are around 2 kJ kg^{-1}. The same is true of the PCIN, shown in Fig. 7c).

The evolution of quantities relevant for this case are shown in Fig. 8. The boundary layer MSE (red line in Fig. 8b) does increase on the day of peak CAPE, but by less than in previous examples. Significantly, it follows a similar diurnal cycle as on previous days (around 10 k J kg^{-1}), controlled primarily by sensible heating (orange line). However, the seen 500-hPa MSE* (blue line in Fig. 8a) decreases significantly starting about 60 h before peak CAPE. The initial drop in seen MSE* occurs when the parcels cross from the Gulf of Mexico to land, then it continues to drop over the next 50 h before the time of peak CAPE. The local 500-hPa MSE* (i.e., at the location of peak CAPE) does not change much over the time period, indicating that it is advection, rather than cooling, that causes this change in seen MSE*. As with the previous examples, the PCAPE (red dashed line in Fig. 8a) is a good but not perfect proxy for CAPE (red solid line), as the two change in the same direction almost all the time, and both quantities have three peaks, each about 24 h apart.

The quantities relevant to the buildup and decrease of CIN are shown in Fig. 8c. Both quantities are somewhat variable in the early period, with a large PCIN for a few hours around −32 h. However, the CIN that is relevant to this high CAPE

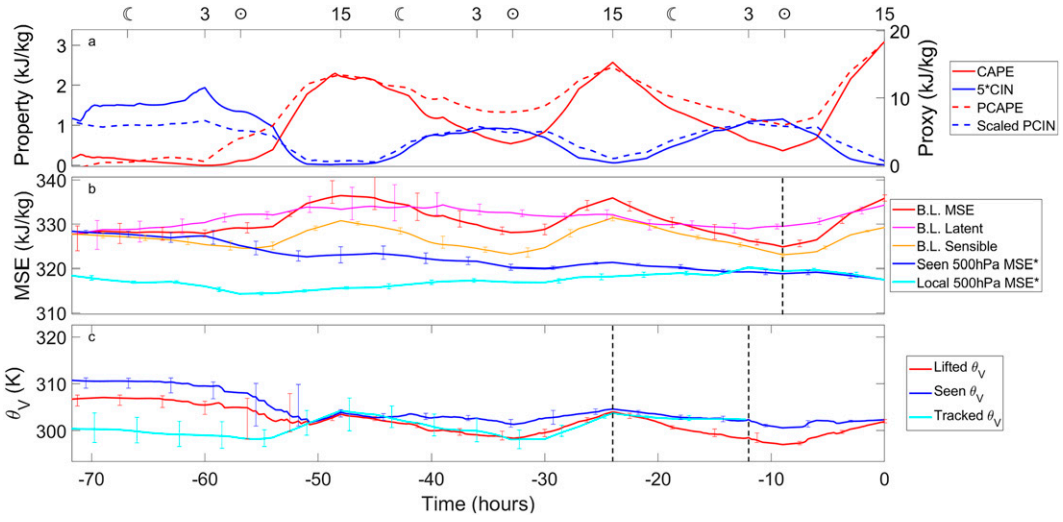

FIG. 8. As in Fig. 4, but for the fourth high CAPE example. In (a), the 500 hPa* at the horizontal location of peak CAPE is also shown, because the change in 500-hPa quantities is relevant for this example.

occurrence (i.e., the CIN shown in Fig. 5c) builds up over the middle period, starting from around −24 h and peaking around −12 h. This increase in CIN is due more to boundary layer cooling than to warming of the capping inversion. Because, during the diurnal cycle, the lifted θ_V decreases by more than the seen θ_V, there is CIN buildup. On the day of peak CAPE, PCIN decreases due to boundary layer warming (i.e., an increase in lifted θ_V). As usual, PCIN is a good proxy for CIN in this example (blue lines in Fig. 8c).

The fifth high CAPE example, in which the boundary layer parcels move south from Canada causing an unusual pattern of CAPE and CIN, is shown in Figs. 9 and 10. About 140 h before the time of high CAPE, the boundary layer parcels were north of 50° latitude, and move south over most of this time before moving slightly north to be over the central United States at the time of peak CAPE (red paths in Fig. 9a). These parcels were around 940 hPa at the time of high CAPE, and were nearly all within 100 hPa of the surface for the 140 h before that. The parcels that form the capping inversion similarly traveled southward, moved toward the surface over the Gulf of Mexico, then moved north and upward to the location of maximum PCIN. Figure 9b shows that there is a relatively small area of some CAPE, almost 1.5 kJ kg^{-1} at the time in question, and Fig. 9c shows that there is a great deal of inhibition over most of North America 12 h before this. There is a small maximum of PCIN at the location of the parcels in question, with a PCIN of about 9 K.

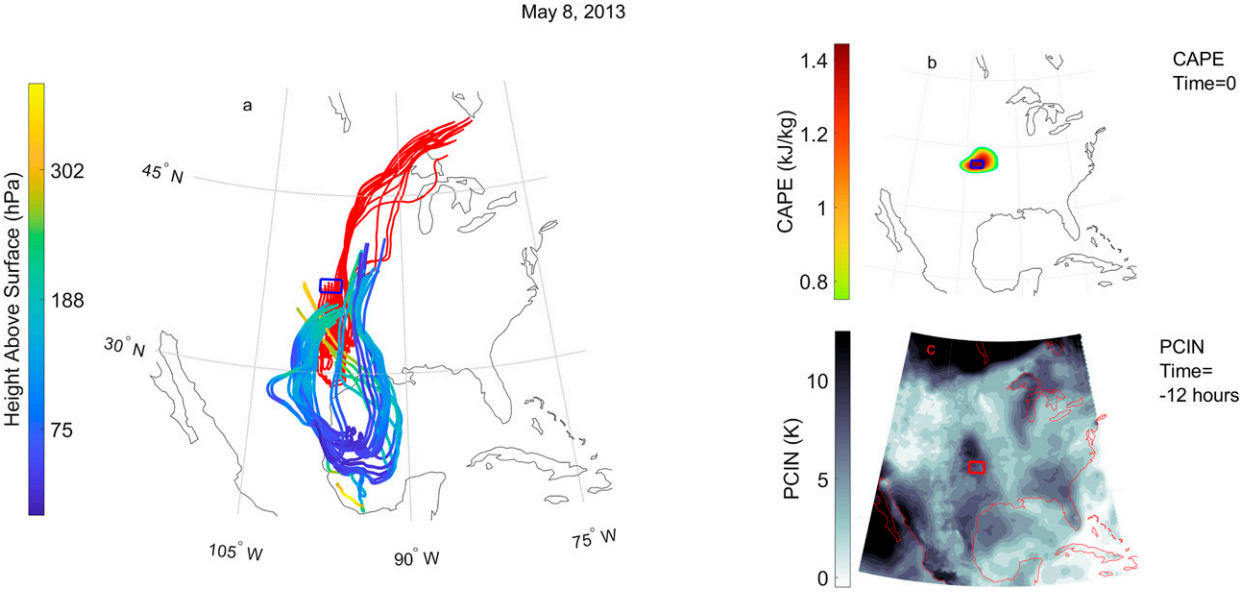

FIG. 9. As in Fig. 1, but for the fifth high CAPE example. The trajectories extend back slightly more than 140 h.

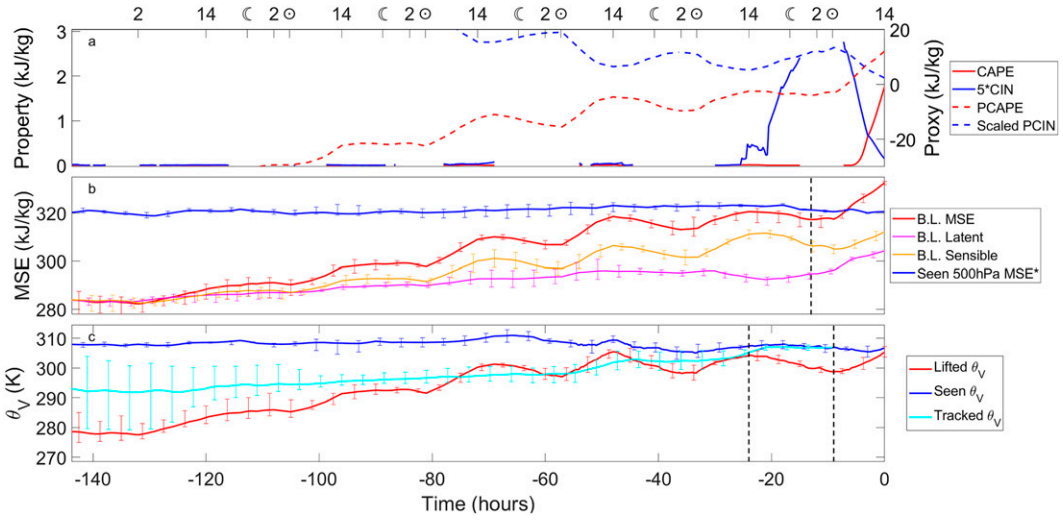

FIG. 10. (a)–(c) As in Fig. 4, but for the fifth high CAPE example. If the lifted parcel is negatively buoyant everywhere in the column, CAPE and CIN are undefined and, therefore, not shown. Unlike in other examples, we here show negative values of PCAPE [in (a)] because it is negative for so much of the time series.

Figure 10 shows the evolution of relevant quantities before this high CAPE occurrence. The boundary layer MSE (Fig. 10b, red) about 140 h before the high CAPE occurrence was barely above 280 kJ kg^{-1}, far smaller than that of the other examples. This makes sense, as the parcels were much further north at the time. Then, over the following 6 days, the boundary layer MSE steadily increases, while undergoing six diurnal cycles. The latent heat increases monotonically and rather consistently (except between −35 and −20 h), while the sensible heat increases while undergoing diurnal cycles. On the day of peak CAPE, the MSE increases by much more than the previous days (more than 10 kJ kg^{-1}), in only 9 h, driven by an additional contribution from latent energy. Over this entire time period, the seen 500-hPa MSE* (blue) is nearly constant. Figure 10a shows the CAPE over time, but it is not particularly meaningful as CAPE is zero when the boundary parcels are negatively buoyant with respect to the entire column. When the CAPE is nonzero, it is very small until the fast increase in boundary layer MSE on the day of high CAPE. Figure 10c shows the quantities relevant to the buildup of CIN. Although CIN is technically undefined for most of the 140 h before the time of high CAPE (solid blue line in Fig. 10a); the lifted θ_V (red line in Fig. 10c) is much smaller than the seen θ_V (blue line) over this time period, indicating that convection could not occur. The lifted θ_V increases steadily from −140 to −22 h, while undergoing a diurnal cycle. Over this time, the seen θ_V is relatively constant. Then, between −22 and −9 h, both the lifted and seen θ_V decrease, with the lifted θ_V decreasing by more, causing an increase in PCIN and therefore CIN buildup. The tracked θ_V increases from −60 to −7 h, indicating that the air in the capping inversion may have been previously warmed by the surface, perhaps when it was over northern Mexico (see Fig. 9). As usual, the decay of the capping inversion on the day of peak CAPE is due to an increase in lifted θ_V from boundary layer heating (after −9 h).

b. *Averages distributions of relevant quantities*

Having presented five examples, we now compare the high CAPE cases with the low CAPE cases and discuss relevant statistics from all cases studied. Figure 11 shows the same quantities as were shown for the sample time series, but compares composites of high and low CAPE cases. The composite evolution of each quantity is calculated as the average across all events in each regime (high and low CAPE) at a given time before the CAPE peak. Times when the CAPE is zero or the CIN is undefined are not included in the calculated average.

The difference in seen at 500-hPa MSE* (Fig. 11b, blue line) is relatively constant over the 100 h before peak CAPE, indicating that it is not advection underneath colder air that causes the difference in CAPE between the high and low CAPE cases. The difference in boundary layer MSE (red line), on the other hand, grows over the 60 h before the peak, following the diurnal cycle for 2 days, then increasing significantly on the day of the peak. This diurnal cycle is mostly due to the difference in sensible heat (orange line), which follows a diurnal cycle, but does not change other than that. The difference in latent energy, on the other hand, increases almost monotonically in the days leading up to peak CAPE, with an especially large and fast increase in the final 12 h. This indicates that the energy difference between strong and weak CAPE cases is largely due to the difference in boundary layer moisture, and that this difference increases dramatically in the 12 h before the peak.

Figure 11a shows how the CAPE and CIN differ between high and low CAPE cases. Note that we do not show how the proxies match the convective properties. The low CAPE cases exhibit a small diurnal cycle, but the CAPE never goes above about 1 kJ kg^{-1}. The high CAPE time series exhibits a significant diurnal cycle, reaching about 1 kJ kg^{-1} the day before the peak and then 2.5 kJ kg^{-1} on the day of the peak. This

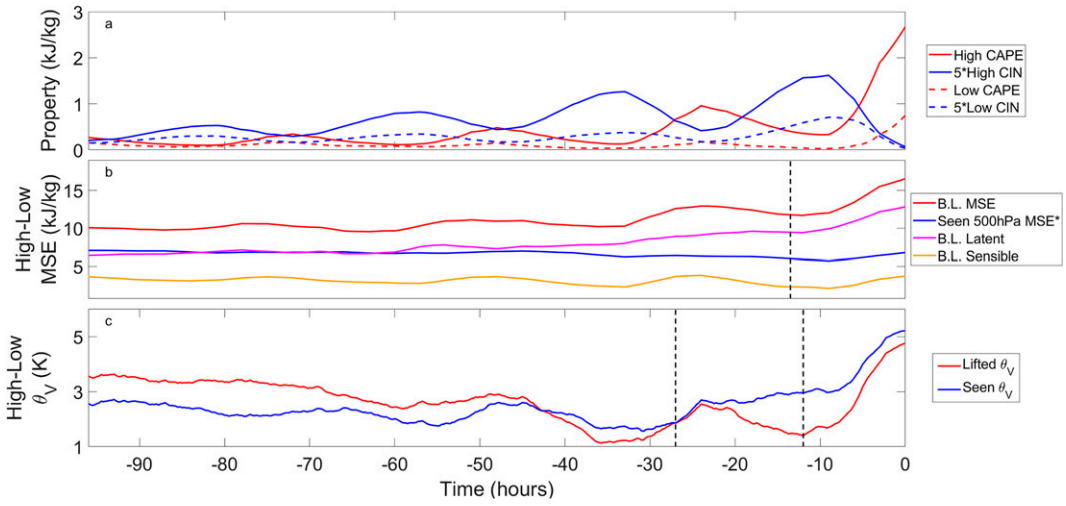

FIG. 11. A comparison of the relevant quantities for high and low CAPE cases in the days leading up to the time of maximum CAPE. (b),(c) Time series of the differences between composites of high and low CAPE cases for the quantities shown in Fig. 2. (a) The CAPE and "5*CIN" averaged across all high (solid) and low (dashed) CAPE cases. CIN is multiplied by 5 for visual ease.

implies that most of the buildup of energy occurs on the day of the event. The CIN time series also differ significantly. The CIN before low CAPE peaks is very small, with a small but notable bump on the night before the event, reaching up to 140 J kg^{-1} (note the factor of 5 on the time series). The composite CIN before the large CAPE peaks, on the other hand, has a significant diurnal cycle for 3 days before the time of peak CAPE. This is especially clear between −30 and −40 h, when CIN reaches over 250 J kg^{-1}, and around −10 h, when it reaches about 320 J kg^{-1}. This implies that the buildup of CIN over the 2 days before the time of peak CAPE is important for allowing this CAPE to buildup, as one would expect.

Figure 11c demonstrates how this vital CIN buildup is different in high and low cases. It is important to note that the PCIN appears to not track the CIN before around −40 h; this is almost certainly due to the CIN being undefined during this time period for several events. When compared to low CAPE cases, we see that the lifted θ_V in high CAPE cases undergoes a significant diurnal cycle. This matches the boundary layer sensible heating, which also exhibits a larger diurnal cycle in high CAPE cases than in low CAPE cases. The boundary layer cooling associated with this diurnal cycle leads to larger PCIN, and therefore CIN, in the high CAPE cases between −30 and −40 h, and after −20 h. During the first of these diurnal cycles (starting around −48 h), the decreases in lifted θ_V difference are accompanied by a decrease in the seen θ_V difference, i.e., although the boundary layer parcels for high CAPE cases are getting colder, so is the air above them. However, this is not true for the last night before the CAPE peaks. During that night, the seen θ_V actually increases for high CAPE cases relative to low CAPE cases. Overall, what differentiates the buildup of CIN in high CAPE cases are two nights of significant boundary layer cooling (with the second being much more important), and a lack of cooling of the capping inversion on the night before the event. Finally, on the day of the CAPE peak, the difference in PCIN between high and low cases nearly disappears due to a very fast increase in lifted θ_V. For the CIN to decay and the CAPE to build up as is seen in high CAPE cases, the partitioning between surface sensible and latent fluxes is of crucial importance. Too much sensible heating would have CIN vanishing before much CAPE had built up; too little and the inhibition might not be overcome before sunset.

Having compared the time evolution of high and low CAPE cases, we now wish to examine the distributions of the relevant quantities. We first examine how the change in PCAPE before the time of maximum CAPE is divided between early and late periods, and between boundary layer and seen, and how the boundary layer MSE changes are partitioned among changes of latent energy and DSE. In reference to the buildup of CIN, we show how the change in PCIN is divided between tracked, lifted, and seen in the middle and late periods, in addition to how long it takes for the PCIN to build up.

Figure 12 presents histograms of relevant quantities for the buildup of CAPE across all events. Figures 12a and 12b show the change in early boundary layer and seen energy, where the difference between these is our proxy for the buildup of CAPE in the early period. For both high CAPE cases (blue boxes and vertical line) and low CAPE cases (red transparent boxes and dashed line), the distributions are centered around zero, indicating that there is not, on average, a significant amount of CAPE buildup in the early period. Figures 12c and 12d show the same quantities for the late period. The late seen MSE* typically does not change in either high or low CAPE regimes, i.e., both distributions are centered around zero (Fig. 12d). The late boundary layer MSE changes, on the other hand, are almost uniformly positive for both high and low CAPE regimes. There is a significant difference between

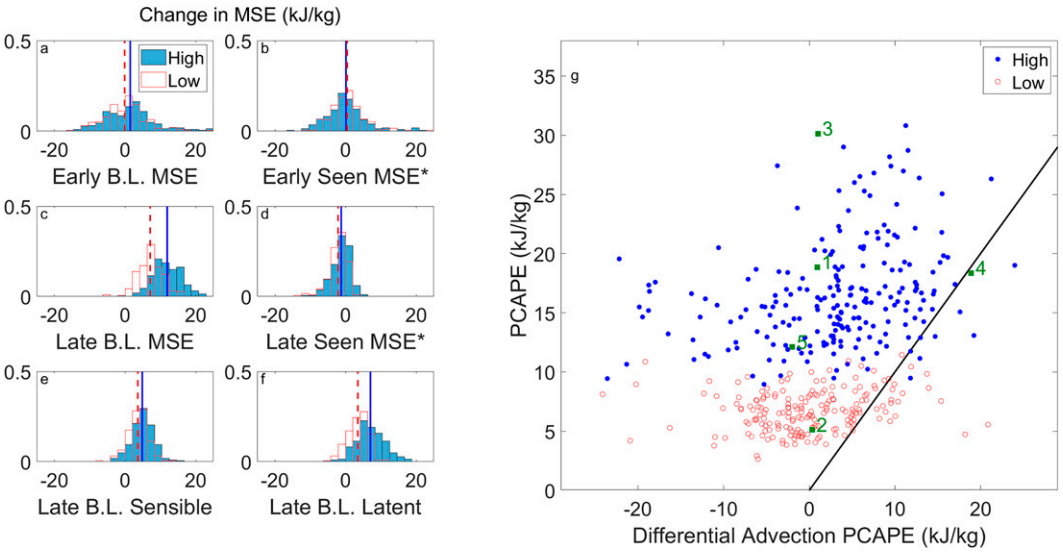

FIG. 12. Distributions of relevant changes in MSE (or MSE*) for each CAPE regime. In each panel, high CAPE cases are shown in solid blue, and low CAPE cases are shown in transparent red. The vertical blue lines represent the average across high CAPE cases, while the dashed red lines represent the average across low CAPE cases. The distribution of changes in MSE (or MSE*) is shown for each of the four components that control PCAPE: (a) early boundary layer, (c) late boundary layer, (b) early seen, and (d) late seen. The "early" changes correspond to the difference in quantities from 24 h before the beginning of CIN buildup to the time of minimum PCAPE, while the "late" changes correspond to the difference in quantities from the time of minimum PCAPE to the time of peak CAPE. In addition, the late boundary layer MSE changes are partitioned into (e) late boundary layer sensible and (f) late boundary layer latent. (g) The role of differential advection in the buildup of PCAPE. Each point corresponds to one CAPE case, with the x coordinate being how large PCAPE would have been if the MSE of the boundary layer parcels had remained constant since the beginning of the early period, and the y coordinate being the observed PCAPE. The green points correspond to the examples discussed above in Figs. 1–10. The black line corresponds to $x = y$.

the boundary layer MSE changes in high CAPE versus low CAPE regimes, with the average boundary layer energy buildup in a high CAPE case being about double that of a low CAPE case, implying that this is the quantity which differentiates high and low CAPE regimes. This increase in late boundary layer MSE can be split into contributions from sensible heating (Fig. 12e) and moistening (Fig. 12f). The sensible heating distributions are centered well above zero for both high and low CAPE cases, with their averages being similar, but with high CAPE cases being slightly larger. The general increase in boundary layer sensible heat is not surprising, as the late period is usually from very early in the day to midafternoon. It is worth noting that this sensible heat increase can be due to an increase in temperature or geopotential height, as the parcels can move up and down along a dry adiabat with no external heating. The boundary layer moistening (Fig. 12f) is also almost always positive for all cases, but for this component, there is a large difference between high and low CAPE cases. This matches the results of Fig. 11, showing that a large contribution to the energy difference between high and low CAPE cases comes from boundary layer moistening on the day of the peak. The correlation between late boundary layer moistening and the final CAPE is 0.46 (p value $< 10^{-3}$), while the correlation between late boundary layer sensible heating and the final CAPE is 0.12 (p value 0.002). Overall, these distributions agree with Fig. 11 that buildup of large CAPE is mostly due to boundary layer moistening on the day of peak CAPE.

To directly compare these results to that predicted by the advection hypothesis, Fig. 12g shows how the observed PCAPE compares to how much PCAPE there would have been with no boundary layer heating or cooling, i.e., if the buildup of CAPE was solely due to differential advection. This "differential advection PCAPE" is calculated as the difference between the boundary layer MSE at the beginning of the early period and the seen MSE* at the time and location of the peak CAPE. According to the advection hypothesis, this would be comparing the energy of surface air over the Gulf of Mexico to cold air aloft over the continent, and this would be the energy difference that causes high CAPE. If this were indeed the source of the observed PCAPE, then events would fall on the "advection hypothesis line" (black line in Fig. 12g), i.e., there would be a strong correlation between the observed PCAPE and the differential advection PCAPE. However, we see that a vast majority of the cases are above the advection hypothesis line, with most events being far above the line. This is true for both high and low CAPE regimes, but the effect is larger for the high CAPE regime (blue points), indicating that boundary layer increases in energy are essential to building up high CAPE. Figure 12g also highlights the examples shown in Figs. 1–10. Example 1, chosen as a typical example, is slightly above the center of the cloud of high CAPE cases. Example 2 is within the normal range for low

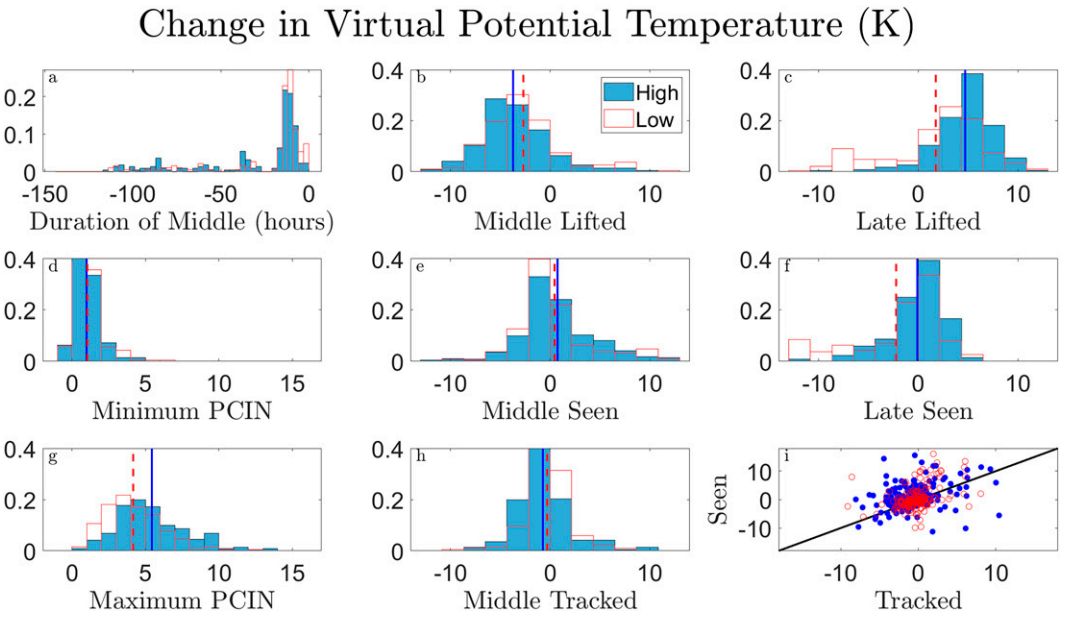

FIG. 13. The distribution of relevant quantities for changes in θ_V for each CAPE regime. (a) The duration of the middle period, or how long the CIN takes to build up. (d),(g) The PCIN on either side of this period, i.e., the minimum and maximum PCIN, respectively. The changes of PCIN are partitioned among six components: (b) middle lifted, (c) late lifted, (e) middle seen, (f) late seen, and (h) middle tracked. (i) A scatterplot of the change in middle seen vs middle tracked and the line $y = x$. In all panels, solid blue represents the high CAPE cases, and the red outline represents the low CAPE cases. The blue vertical lines represent the average across all high CAPE cases, while the dashed red lines represent the average across all low CAPE cases.

CAPE cases, although its final PCAPE is slightly smaller than average. Examples 3 and 4 were chosen as examples with very important and unimportant boundary layer heating, respectively, so they are very far above the advection hypothesis line and slightly below the line, respectively. Example 5, which was chosen for its unusual behavior of CAPE and CIN, is also well above the line, as its boundary layer MSE started quite low and increased over the tracking period.

Figure 13 presents statistics on the buildup of PCIN. Figure 13a shows the duration of the middle period, i.e., how long it takes CIN to build up (defined in section 2). We see that this duration is typically less than 24 h, and since the time of maximum PCIN is almost always the night before the day of peak CAPE, this implies that CIN builds up from the day before peak CAPE to the night before. There are events where CIN buildup takes an extra day (such as the first example shown above) or even longer (such as the second example), but these are atypical. Note that this is true for both high and low CAPE cases (blue solid, and red transparent, respectively). This does not mean that there was no CIN two nights before peak CAPE (see Fig. 11), just that it disappears and reappears during the night before peak CAPE for most events. Figures 13b,e,h show the distributions of changes in lifted, seen, and tracked θ_V during the middle period (CIN buildup), for both high and low CAPE cases. We see that the lifted parcels cool over this time period in both high and low CAPE regimes, but the lifted parcels in high CAPE cases cool more. There is also a small difference in the change of seen θ_V over the course of the middle period, with the high CAPE cases increasing by slightly more. Figures 13d,g show the amount of PCIN at the beginning (Fig. 13d) and end (Fig. 13g) of the middle period. Although both the high and low CAPE cases start with very little PCIN (about 1 K), the high CAPE cases end up with far more convective inhibition than the low CAPE cases. These, together with the distributions in Figs. 13b,e, tell us that high CAPE cases tend to have more CIN than usual on the night before the CAPE peak, and that this is usually due to anomalously strong boundary layer cooling. This matches the features shown in Fig. 11. Figures 13c,f show how CIN disappears on the day of peak CAPE, and unsurprisingly, we see that the distribution of changes in late lifted θ_V is centered well above zero, and its average is larger for high CAPE cases than for low CAPE cases. In other words, boundary layer heating is what allows a column to overcome the convective inhibition. Figures 13h,i show the features of the tracked parcels, i.e., the ones that form the capping inversion. Figure 13h shows how θ_V of the tracked parcels change over the middle period, and Fig. 13i shows how this change is correlated with that of the seen parcels. These quantities are both centered around zero (Figs. 13e,h) in both high and low CAPE cases, but they are not correlated (Fig. 13i), indicating that the properties above the boundary layer parcels are controlled by advection, not warming or cooling of the parcels that are above them at the time.

4. Conclusions

We here presented examples and statistics of the properties of air parcels leading up to states of anomalously high CAPE.

We showed that nearly all of the CAPE buildup before extreme CAPE peaks is due to boundary layer heating, and that most of this heating is due to moistening in the days leading up to the time of maximum CAPE, principally on the day of peak CAPE. For this moistening to occur without shallow convection releasing any potential energy, there needs to be a large amount of CIN during the CAPE buildup. This increase of CIN usually happens during the night before the CAPE peak, and is due mostly to boundary layer cooling during the diurnal cycle with a small contribution from advection underneath unusually warm air. There is then a decrease in CIN on the day of anomalously high CAPE which, similar to the increase in CAPE, is almost entirely due to boundary layer heating. This evidence disagrees strongly with the advection hypothesis, which holds that the buildup of CAPE is due to a decrease in seen MSE^*. There is also recent evidence against the advection hypothesis from simulations, as Li et al. (2021) found that replacing the Gulf of Mexico with land did not significantly change the amount of CAPE over North America in a CAM6 atmospheric simulation.

These conclusions have substantial implications for the climatology of CAPE, and suggest that the impact of surface fluxes on the buildup of CAPE (although beyond the scope of this study) may be a promising area of future research. Since the accumulation of CAPE that occurs within the 12 h before the time of peak CAPE and reduction of CIN are due to boundary layer heating, and the MSE of air parcels is mostly conserved in the absence of radiation and surface fluxes, it is highly likely that soil properties (e.g., albedo and moisture) along the trajectory are of great importance to the occurrence of severe convective events, as they determine net surface enthalpy flux and its partition between latent energy and DSE increases following an air parcel. It also seems to be the case that unusually large CAPE follows unusually large nocturnal cooling, which may be related to increased outgoing longwave radiation due to anomalously dry air aloft (not shown in this study).

As shown by Agard and Emanuel (2017), among others, the evolution of CAPE and CIN depends crucially on solar heating, surface wind speed, and the Bowen ratio, which in turn depends on soil moisture. It is likely that for a given magnitude of CIN and solar heating, there is an "ideal" Bowen ratio for the outbreak of severe convection. The wetter the soil, the greater the buildup of CAPE, but there may not be enough sensible heating to overcome the CIN before sunset. If the soil is too dry, on the other hand, the CIN may be eroded before there has been appreciable buildup of CAPE.

There are many variations on this theme, however. For example, if there has not been enough surface sensible heat flux to overcome the existing CIN during daylight hours, the air comprising the capping inversion may later undergo ascent, even at night, eroding the CIN and releasing the CAPE that accumulated previously.

These results suggest that good forecasts of short-term evolution of CAPE and CIN depend, among other things, on high quality boundary layer schemes and good initialization of soil properties, especially soil moisture. The analysis and prediction of soil moisture may also be key to seasonal prediction of severe convective activity. Given the existing intermodel spread in predictions of the response of precipitation and evaporation to climate change, good predictions of soil moisture may prove challenging. The simple boundary layer model developed by Agard and Emanuel (2017) predicts that as the soil temperature rises, holding soil wetness, insolation, and surface wind speed constant, peak values of CAPE and CIN should both increase, but this conclusion may be altered by changing insolation, soil moisture and albedo, and/or surface wind speeds.

A crucial aspect of severe convection that is not discussed here is the connection between CAPE and the occurrence of observed severe weather. It has been conclusively shown (e.g., Grams et al. 2012) that CAPE alone is not enough to cause severe convection; sufficient wind shear and a trigger are also vital, and that there are cases where severe convection occurs in low CAPE environments (e.g., Sherburn and Parker 2014). In our dataset, about 80% of the high CAPE occurrences identified were nearby and on the same day as a severe convective event reported by National Weather Service's Storm Prediction Center. However, our technique of Lagrangian tracking of relevant parcels, and the understanding that boundary layer heating and cooling are vital to the buildup of CAPE, can be easily applied to cases where severe convection was observed, even in high-shear low-CAPE cases. Understanding how large values of CAPE are achieved is an important, if insufficient, step in understanding the climatology of severe convection.

Acknowledgments. K. Emanuel was supported by the National Science Foundation under Grant AGS-1906768. P. Tuckman was supported by the Rasmussen Fellowship, a graduate fellowship for the department of Earth, Atmospheric, and Planetary Sciences at MIT. This work was largely inspired by the Ph.D. thesis and an unpublished manuscript of V. Agard, who was supported by the Office of Naval Research under Award N00014-14-1-0062. We also thank the reviewers for their helpful comments on this work.

Data availability statement. The reanalysis data used for this article can be accessed on the North American Regional Reanalysis website (https://psl.noaa.gov/data/gridded/data.narr.html) and the severe weather reports can be accessed on the National Weather Service's Storm Prediction Center website (https://www.spc.noaa.gov/).

APPENDIX A

Discussion of NARR Dataset

It has been previously shown that some issues arise in the use of the NARR dataset to study severe thunderstorm environments (e.g., Gensini et al. 2014). Specifically, it has been shown that NARR low-level moisture fields often disagree with

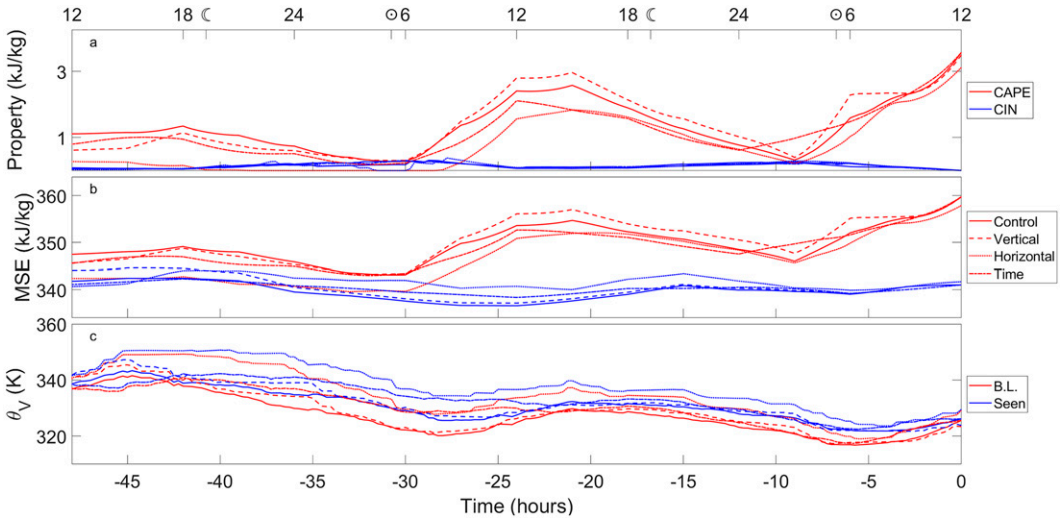

FIG. A1. The effect of resolution on relevant time series for the example shown in Figs. 1 and 2. For each time series, the control (solid), decreased vertical resolution (dashed), decreased horizontal resolution (dotted), and decreased time resolution (dash–dotted) are shown. (a) The red lines correspond to CAPE, while the blue lines correspond to CIN. (b) The red lines correspond to boundary layer MSE, while the blue lines correspond to seen 500 hPa MSE*. (c) The red lines correspond to lifted θ_V, while the blue lines correspond to seen θ_V at the altitude of maximum θ_V difference.

that of soundings. Although this may be an issue, we are mostly concerned with the change in low-level moisture of parcels of air, so any systematic and regional biases are unlikely to significantly affect our main conclusions. Also, we follow the recommendation given in Gensini et al. (2014) to use a single near-surface level to calculate CAPE rather than average over the mixed layer. We avoid using the surface level data because the wind speeds are too small to adequately represent how boundary layer parcels are moving.

In addition, the resolution of the NARR dataset may be a concern. This is certainly an issue when comparing reanalysis data to soundings (as in Gensini et al. 2014), because soundings are taken at one point in space, while reanalysis data represent an average over a grid cell. To test resolution sensitivity, we demonstrate that artificially coarsening the resolution of the NARR dataset does not significantly affect the results. This suggests that we have converged to a resolution that is fine enough to justify our main conclusions. We also briefly discuss our use of a Lagrangian tracking time step much smaller than the time step of 3 h in NARR output.

The resolution of the NARR dataset is artificially reduced in three different ways. First, the vertical resolution is decreased by simply ignoring every other pressure level (starting with 975 hPa). Second, to decrease the horizontal resolution, every other data point in both the x and y direction is ignored—meaning there are a total of one quarter as many data points in the horizontal. Finally, to decrease the time resolution, the data point immediately before the time of maximum CAPE, as well as every other time point before that, are ignored. The results of these resolution decreases (enacted one at a time) are shown in Figs. A1 and A2.

Figure A1 shows the effect of decreasing resolution on the relevant quantities for the typical high CAPE case shown originally in Fig. 2. The effect of changing the horizontal resolution is small, with a few noticeable differences between the control (solid lines) and decreased horizontal resolution runs (dotted lines). Most notably, θ_V for both the boundary

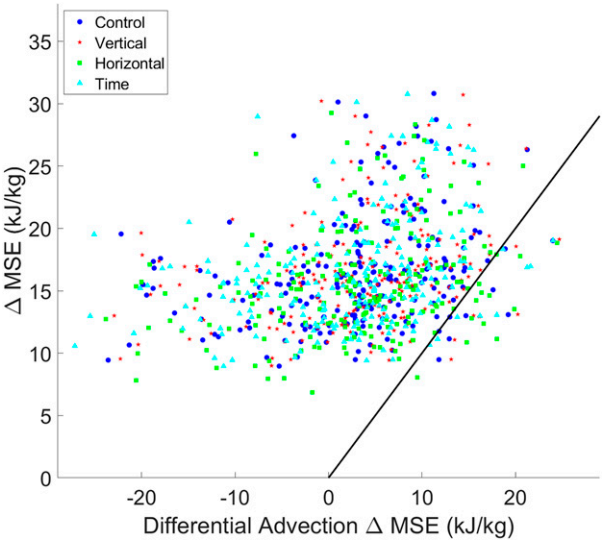

FIG. A2. As in Fig. 12g, but varying the resolution of the dataset used. The blue dots show the same data as in Fig. 12g, the red stars correspond to decreased vertical resolution, the green squares correspond to decreased horizontal resolution, and the cyan triangles correspond to decreased time resolution. Only the high CAPE cases are shown.

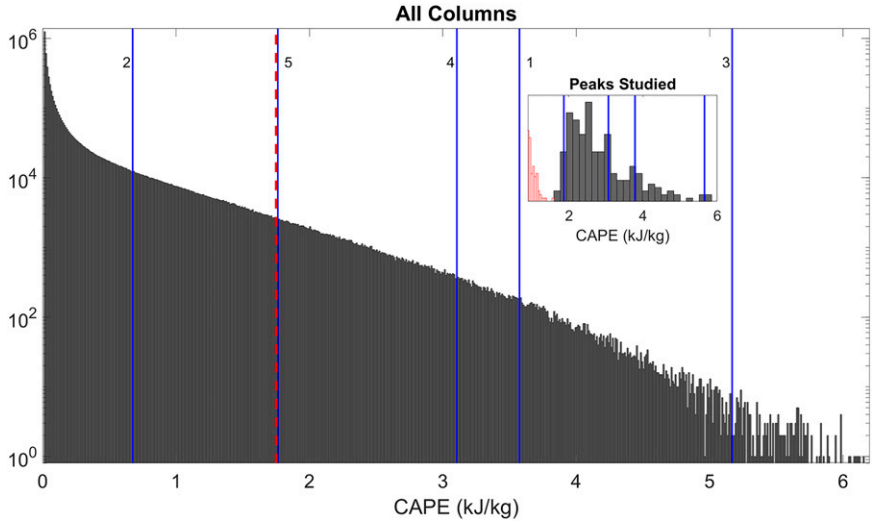

FIG. B1. Histogram of calculated (smoothed) CAPE in all columns (main plot) and peaks chosen as the endpoints for trajectories studied (subplot). The blue lines (labeled in the main plot) correspond to the examples discussed in Figs. 1–10. The red dashed line corresponds to the threshold used to choose CAPE peaks of interest. As in Fig. 12, the red outlined boxes represent the low CAPE cases, and the solid boxes represent the high CAPE cases.

layer and seen parcels are larger when the horizontal resolution is decreased, but the difference between them, the relevant property for convection, is similar to the control case. Decreasing the vertical resolution (dashed lines) has a slightly larger effect, making the CAPE (red lines in Fig. A1b) somewhat larger between 8 and 3 h before the event, but does not have any other significant effects. Altering the time resolution (dash–dotted lines) has perhaps the most significant influence for our purposes, shifting the beginning of the boundary layer MSE increase (and therefore the CAPE increase) about 3 hours earlier. The seen 500-hPa MSE* (blue lines in Fig. A1a), the CIN (blue lines in Fig. A1a), and the seen θ_V (blue line in Fig. A1c) do not change significantly with the change of resolution. Overall, changing the resolution can alter the quantities somewhat, but does not change the overall conclusions drawn about this event, i.e., that the buildup of CAPE is due to an increase in boundary layer MSE and that the buildup of CIN is due to cooling of the lifted θ_V.

Next, we wish to check if decreasing the resolution of the NARR dataset affects the major conclusions discussed in the main text. To this end, we compare the data shown in Fig. 12g to the same data calculated with reduced resolution in Fig. A2. Changing the resolution in the three ways discussed above does not systematically change the conclusions reached, i.e., the observed MSE differences are still due to boundary layer warming, as a vast majority of the points are above the "advection hypothesis line" discussed in reference to Fig. 12g.

Overall, decreasing the resolution of the NARR dataset by a factor of 2 does not significantly affect our conclusions. The fact that linearly interpolating between the coarsened data points does not alter the results implies that the data are roughly linear on those spatial and temporal scales. This means that linearly interpolating between the finer data points, as we did for the majority of the study, is valid. Similarly, the lack of temporal nonlinearity implies that the fields can be treated as roughly linear with respect to the Lagrangian time steps chosen (15 min). Since the fields change roughly linearly on the time scale chosen, we are not acquiring significant errors by linearly interpolating to times 15 min apart.

Despite these reasons for the validity of using NARR for this study, it would be useful to run the same type of analysis with other datasets. The temporal and spatial sparseness of rawinsondes makes it impractical to use them directly for trajectory calculations. However, there are other reanalysis datasets that could be used to check the results shown here.

APPENDIX B

CAPE Frequency Distribution

Here we discuss the distribution of CAPE in the columns studied and the high CAPE occurrences chosen for study. Figure B1 shows the distribution of CAPE across all columns, i.e., from March through August of 2012 and 2013 in the region of the NARR dataset (latitude between 36° and 67°, longitude between −120° and −74°). Altogether, about 221 columns studied are above the threshold chosen (1.75 kJ kg^{-1}), and 188 were chosen as "low CAPE cases," i.e., CAPE between 0.75 and 1 kJ kg^{-1}. This threshold corresponds to the middle of CAPE values for severe convection over land (Grams et al. 2012), but not so low that there are an unreasonable number of cases to study. It is worth noting that severe convection depends on a

combination of CAPE and wind shear (Brooks et al. 2003), but here we concern ourselves only with the factors that lead to high CAPE. The examples chosen for this study are marked by solid blue lines. The first example is one of the higher CAPE occurrences, the second example is far below the threshold for "high CAPE," the third example is the highest CAPE occurrence in the dataset, the fourth example is in the middle range of cases studied, and the fifth example is just above the threshold of 1.75 kJ kg^{-1}.

REFERENCES

Agard, V., and K. Emanuel, 2017: Clausius–Clapeyron scaling of peak CAPE in continental convective storm environments. *J. Atmos. Sci.*, **74**, 3043–3054, https://doi.org/10.1175/JAS-D-16-0352.1.

Allen, J. T., 2018: Climate change and severe thunderstorms. *Climate Science*, H. von Storch, Ed., Oxford University Press, https://doi.org/10.1093/acrefore/9780190228620.013.62.

——, M. K. Tippett, and A. H. Sobel, 2015: Influence of the El Niño/Southern Oscillation on tornado and hail frequency in the United States. *Nat. Geosci.*, **8**, 278–283, https://doi.org/10.1038/ngeo2385.

Bluestein, H. B., 2007: Advances in applications of the physics of fluids to severe weather systems. *Rep. Prog. Phys.*, **70**, 1259, https://doi.org/10.1088/0034-4885/70/8/R01.

Botzen, W. J. W., L. M. Bouwer, and J. C. J. M. van den Bergh, 2010: Climate change and hailstorm damage: Empirical evidence and implications for agriculture and insurance. *Resour. Energy Econ.*, **32**, 341–362, https://doi.org/10.1016/j.reseneeco.2009.10.004.

Bouwer, L. M., 2011: Have disaster losses increased due to anthropogenic climate change? *Bull. Amer. Meteor. Soc.*, **92**, 39–46, https://doi.org/10.1175/2010BAMS3092.1.

Brooks, H. E., 2013: Severe thunderstorms and climate change. *Atmos. Res.*, **123**, 129–138, https://doi.org/10.1016/j.atmosres.2012.04.002.

——, C. A. Doswell III, and M. P. Kay, 2003: Climatological estimates of local daily tornado probability for the United States. *Wea. Forecasting*, **18**, 626–640, https://doi.org/10.1175/1520-0434(2003)018<0626:CEOLDT>2.0.CO;2.

——, G. W. Carbin, and P. T. Marsh, 2014: Increased variability of tornado occurrence in the United States. *Science*, **346**, 349–352, https://doi.org/10.1126/science.1257460.

Cao, Z., 2008: Severe hail frequency over Ontario, Canada: Recent trend and variability. *Geophys. Res. Lett.*, **35**, L14803, https://doi.org/10.1029/2008GL034888.

Carlson, T. N., and F. H. Ludlam, 1968: Conditions for the occurrence of severe local storms. *Tellus*, **20**, 203–226, https://doi.org/10.1111/j.2153-3490.1968.tb00364.x.

——, S. G. Benjamin, G. S. Forbes, and Y.-F. Li, 1983: Elevated mixed layers in the regional severe storm environment: Conceptual model and case studies. *Mon. Wea. Rev.*, **111**, 1453–1474, https://doi.org/10.1175/1520-0493(1983)111<1453:EMLITR>2.0.CO;2.

Changnon, S. A., 2009: Increasing major hail losses in the U.S. *Climatic Change*, **96**, 161–166, https://doi.org/10.1007/s10584-009-9597-z.

Cook, A. R., L. M. Leslie, D. B. Parsons, and J. T. Schaefer, 2017: The impact of El Niño–Southern Oscillation (ENSO) on winter and early spring U.S. tornado outbreaks. *J. Appl. Meteor. Climatol.*, **56**, 2455–2478, https://doi.org/10.1175/JAMC-D-16-0249.1.

Del Genio, A. D., M.-S. Yao, and J. Jonas, 2007: Will moist convection be stronger in a warmer climate? *Geophys. Res. Lett.*, **34**, L16703, https://doi.org/10.1029/2007GL030525.

Dessens, J., 1995: Severe convective weather in the context of a nighttime global warming. *Geophys. Res. Lett.*, **22**, 1241–1244, https://doi.org/10.1029/95GL00952.

Diffenbaugh, N. S., M. Scherer, and R. J. Trapp, 2013: Robust increases in severe thunderstorm environments in response to greenhouse forcing. *Proc. Natl. Acad. Sci. USA*, **110**, 16 361–16 366, https://doi.org/10.1073/pnas.1307758110.

Emanuel, K. A., 1994: *Atmospheric Convection*. Oxford University Press, 580 pp.

Gensini, V. A., and T. L. Mote, 2015: Downscaled estimates of late 21st century severe weather from CCSM3. *Climatic Change*, **129**, 307–321, https://doi.org/10.1007/s10584-014-1320-z.

——, ——, and H. E. Brooks, 2014: Severe-thunderstorm reanalysis environments and collocated radiosonde observations. *J. Appl. Meteor. Climatol.*, **53**, 742–751, https://doi.org/10.1175/JAMC-D-13-0263.1.

Grams, J. S., R. L. Thompson, D. V. Snively, J. A. Prentice, G. M. Hodges, and L. J. Reames, 2012: A climatology and comparison of parameters for significant tornado events in the United States. *Wea. Forecasting*, **27**, 106–123, https://doi.org/10.1175/WAF-D-11-00008.1.

Hoogewind, K. A., M. E. Baldwin, and R. J. Trapp, 2017: The impact of climate change on hazardous convective weather in the United States: Insight from high-resolution dynamical downscaling. *J. Climate*, **30**, 10 081–10 100, https://doi.org/10.1175/JCLI-D-16-0885.1.

Kunkel, K. E., and Coauthors, 2013: Monitoring and understanding trends in extreme storms: State of knowledge. *Bull. Amer. Meteor. Soc.*, **94**, 499–514, https://doi.org/10.1175/BAMS-D-11-00262.1.

Li, F., D. R. Chavas, K. A. Reed, N. Rosenbloom, and D. T. Dawson II, 2021: The role of elevated terrain and the Gulf of Mexico in the production of severe local storm environments over North America. *J. Climate*, **34**, 7799–7819, https://doi.org/10.1175/JCLI-D-20-0607.1.

Mesinger, F., and Coauthors, 2006: North American Regional Reanalysis. *Bull. Amer. Meteor. Soc.*, **87**, 343–360, https://doi.org/10.1175/BAMS-87-3-343.

Riemann-Campe, K., K. Fraedrich, and F. Lunkeit, 2009: Global climatology of Convective Available Potential Energy (CAPE) and Convective Inhibition (CIN) in ERA-40 reanalysis. *Atmos. Res.*, **93**, 534–545, https://doi.org/10.1016/j.atmosres.2008.09.037.

Romps, D. M., J. T. Seeley, D. Vollaro, and J. Molinari, 2014: Projected increase in lightning strikes in the United States due to global warming. *Science*, **346**, 851–854, https://doi.org/10.1126/science.1259100.

Rosenzweig, C., F. N. Tubiello, R. Goldberg, E. Mills, and J. Bloomfield, 2002: Increased crop damage in the U.S. from excess precipitation under climate change. *Global Environ. Change*, **12**, 197–202, https://doi.org/10.1016/S0959-3780(02)00008-0.

Schär, C., D. Lüthi, U. Beyerle, and E. Heise, 1999: The soil–precipitation feedback: A process study with a regional climate model. *J. Climate*, **12**, 722–741, https://doi.org/10.1175/1520-0442(1999)012<0722:TSPFAP>2.0.CO;2.

Seeley, J. T., and D. M. Romps, 2015: The effect of global warming on severe thunderstorms in the United States. *J. Climate*, **28**, 2443–2458, https://doi.org/10.1175/JCLI-D-14-00382.1.

Sherburn, K. D., and M. D. Parker, 2014: Climatology and ingredients of significant severe convection in high-shear, low-CAPE environments. *Wea. Forecasting*, **29**, 854–877, https://doi.org/10.1175/WAF-D-13-00041.1.

Trapp, R. J., and K. A. Hoogewind, 2016: The realization of extreme tornadic storm events under future anthropogenic climate change. *J. Climate*, **29**, 5251–5265, https://doi.org/10.1175/JCLI-D-15-0623.1.

——, N. S. Diffenbaugh, H. E. Brooks, M. E. Baldwin, E. D. Robinson, and J. S. Pal, 2007: Changes in severe thunderstorm environment frequency during the 21st century caused by anthropogenically enhanced global radiative forcing. *Proc. Natl. Acad. Sci. USA*, **104**, 19 719–19 723, https://doi.org/10.1073/pnas.0705494104.

Yang, G., and C. Shu, 1985: Large-scale environmental conditions for thunderstorm development. *Adv. Atmos. Sci.*, **2**, 508–521, https://doi.org/10.1007/BF02678749.